AUT Journal of Mechanical Engineering

AUT J. Mech. Eng., 6(4) (2022) 525-544
DOI: 10.22060/ajme.2019.16343.5815

Stability Analysis of a Functionally Graded Carbon Nanotube Reinforced Composite Plate Integrated with Piezoelectric Layers under Supersonic Airflow

M. Hosseini*, K. Majidi Mozafari

Department of Mechanical Engineering, Sirjan University of Technology, Sirjan, Iran

ABSTRACT: The dynamic and static instabilities of plates reinforced by carbon nanotubes which are fully covered by two piezoelectric layers subjected to supersonic airflow are investigated. For aero-elastic analysis of thin functionally graded carbon nanotube reinforced composite plate, classical plate theory, as well as first-order piston theory, has been applied. The effective material properties of functionally graded carbon nanotube-reinforced composite plates are evaluated based on the rule of mixture with consideration of efficiency parameter. Also, five various types of carbon nanotube distributions through the thickness direction are investigated. The distribution of electric potential across the piezoelectric thickness is assumed to be a quadratic function. Then, two kinds of electric boundary conditions such as open circuit and closed circuit are considered. The coupled governing electro-mechanical equations are derived by using Hamilton's variation principle and electrostatic Maxwell's equation. The partial differential governing equations are transformed into a set of ordinary differential equations by utilizing Galerkin's approach. The result shows that the functionally graded carbon nanotube-reinforced composite plate integrated by two piezoelectric layers in open circuit condition has higher both flutter aerodynamic pressure and natural frequencies, in contrast with a similar plate in closed circuit conditions. In addition, the result elucidated that the stability region increase as the piezoelectric thickness increases.

Review History:

Received: May, 15, 2019
Revised: Aug, 17, 2019
Accepted: Sep. 22, 2019
Available Online: Oct. 03, 2019

Keywords:

Aero-elastic
Carbon nanotube
Composite plates
Piezoelectric layers
First-order piston theory

1- Introduction

Nowadays, Carbon Nanotubes (CNTs) are well known for their special properties such as high elastic modulus, high tensile strange, and high stiffness. Then, for the sake of the extraordinary physical and mechanical properties of CNTs, they have become a promising candidate for the reinforcement of nanocomposites [1, 2]. Nanocomposites are composed of the polymer matrix and CNTs as a reinforcement. As reported by Hu et al. [3], the mechanical properties of carbon nanotube-reinforced composites are noticeably improved by adding the CNTs even at very low volume fractions in the polymer matrix. The distribution of CNTs in the polymer matrix may be Functionally Graded (FG) or Uniformly Distributed (UD). Therefore, the material properties vary continuously from one surface to the other. Up to now, a large body of literature has investigated the mechanical behaviors of Functionally Graded CNT Reinforced Composite (FG-CNTRC) plates and shells. The study on the nonlinear bending of simply supported FG-CNTRC plate which reinforced by Single-Walled Carbon Nanotubes (SWCNTs) under transverse load in the thermal environment is performed by Shen [4] based on the Higher-order Shear Deformation Theory (HSDT) and using perturbation technique. Static and free vibration of FG-CNTRC thick plate examined by Zhu et al. [5] based on the first shear deformation theory and using the finite element method. Buckling analysis of FG-CNTRC plates subjected to various mechanical loads is investigated by Lei et al. [6] according to First-order Shear Deformation Theory (FSDT) and using element free KP-Ritz method. In another investigation, Lei et al. [7] studied the free vibration analysis of FG-CNTRC plates reinforced by SWCNTs based on the FSDT and using element free KP-Ritz approach. Wang et al. [8] presented a semi-analytical buckling and free vibration analysis of FG-CNTRC plates based on the Classical Plate Theory (CPT).

Recently, piezoelectric materials have attracted a significant amount of attention from researchers due to their electromechanical coupling. Wu et al. [9] analyzed the free vibration of a circular Kirchhoff plate enclosed by piezoelectric layers with open circuit condition analytically. Farsangi et al. [10] presented an analytical solution for free vibration analysis of a rectangular plate embedded with piezoelectric layers, based on the FSDT and using the Levy solution method. Kiani [11] analyzed the free vibration behavior of FG-CNTRC plates with integrated piezoelectric layers at the top and bottom surfaces, based on the FSDT and Chebyshev-Ritz technique. The aero-thermo-elastic analysis and active flutter control of FG-CNTRC panels using a piezoelectric sensor and actuator based on Reddy's third-order shear deformation theory and assumed mode method

*Corresponding author's email: hosseini@sirjantech.ac.ir

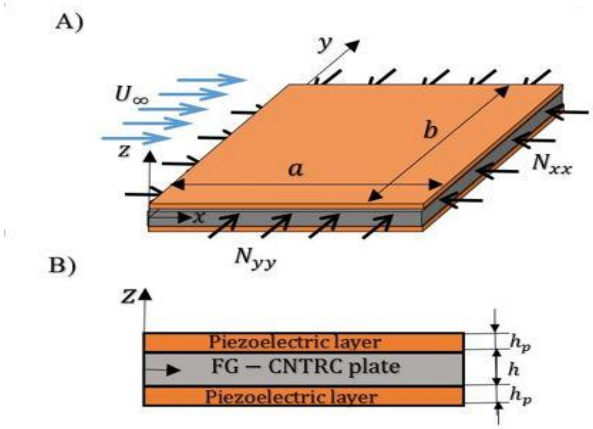

Fig. 1. FG-CNTRC plate enclosed by piezoelectric layers in supersonic airflow a) perspective view, b) front view.

are studied by Zhang et al. [12]. In their investigation, they optimized the area and location of piezoelectric patches through the use of a genetic algorithm. Active vibration control of FG-CNTRC rectangular plate integrated with piezoelectric layers examined by Selim et al. [13] based on Reddy's shear deformation theory.

The aero-elastic characteristics of plates and shells are a serious factor in the design of space re-entry vehicles, high-speed aircraft, and modern engineering applications. In this regard, many researchers have extensively studied the aero-elastic properties of plates and shells. The influence of flow yaw angle, temperature, and aerodynamic damping on supersonic flutter of isotropic and composite plates are investigated by Cheng et al. [14], based on Von-Karman's large deflection theory and using Finite Element Method (FEM). Navazi and Haddadpour [15] researched the aero-thermo-elastic stability analysis of panels made by Functionally Graded Material (FGM), based on CPT and using Galerkin's approach. The static and dynamic stabilities of FGM panels subjected to aero-thermo-elastic loading are investigated by Sohn and Kim [16], based on FSDT in conjunction with nonlinear von-Karman strain displacement and using FEM. Hosseini and Fazelzadeh [17] analyzed the aero-thermo-elastic and vibration behavior of FGM panels using nonlinear von-Karman strain displacement as well as Galerkin's method. A review on the aero-elastic characteristics of FGM panel under supersonic flow was presented by Marzocca et al. [18]. Song and Li [19] analyzed the aero-thermo-elastic characteristics of a supersonic panel flutter with different boundary conditions based on CPT. Dynamic and static stability analysis of FG-CNTRC plates subjected to supersonic airflow is studied by Fazelzadeh et al. [20] according to CPT and using Galerkin's method. Song et al. [21] investigated the aero-elastic analysis of FG-CNTRC plates in supersonic airflow based on the HSDT and state-space Levy solution.

The goal of the current paper is to investigate the effect of piezoelectric layer thickness on the aero-elastic behavior of the FG-CNTRC plate embedded with piezoelectric layers under supersonic airflow. The pressure induced due to supersonic airflow is modeled by first-order piston theory. Here, five different types of CNTs distribution in the thickness direction are considered. The effective material properties are evaluated by using the rule of mixture. The variation of the electric potential across the piezoelectric layer thickness is simulated through the use of a quadratic function. It is supposed, the FG-CNTRC plate integrated with piezoelectric layers is movable and simply supported on all four edges, and two open and closed circuit electric boundary condition of the piezoelectric layer are considered. The coupled mechanical and electrical governing equations are obtained based on the extended Hamilton's principle and Maxwell's equation, respectively. Galerkin's method is applied to convert the coupled partial differential equations into a set of ordinary differential equations. To check the validity of the present research, the results are compared with the available literature. The influence of CNTs volume fraction, CNTs distribution patterns, different piezoelectric material, piezoelectric thickness in both open and closed circuit electric boundary conditions, and in-plane forces on the dynamic and static boundary stabilities are elucidated. Thus the novelties have been listed as:

Investigating the application of the piezoelectric layers on the dynamic stability boundaries of FG-CNTRC plate

Investigating the application of the piezoelectric layers on the static stability boundaries of the FG-CNTRC plate.

Investigating the application of the piezoelectric layers on the critical frequency of the FG-CNTRC plate.

Investigating effects of the material piezoelectric layers on the flutter stability boundaries of FG-CNTRC.

2- Model Strategy and Basic Equations

2- 1- Configuration of the physical system

The schematic of a rectangular FG-CNTRC plate which is fully covered by piezoelectric layers on its top and bottom surfaces is presented in Fig. 1. The origin coordinate system is sitting on the mid-plane of the plates. The plate has the length

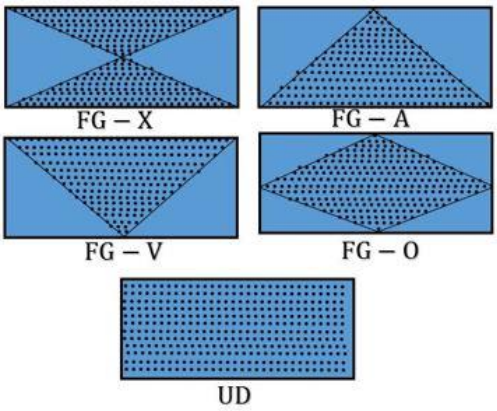

Fig. 2. Distribution patterns of CNTs in the polymer matrix

a, width b, thickness h, and piezoelectric layer thickness h_p. The in-plane force N_{xx} and N_{yy} are exerted to the plate in the x and y direction, respectively. The supersonic airflow is passed over the top surface of the plate with free stream velocity U_∞.

2- 2- Material properties of FG-CNTRC plates

The plate is made from a mixture of the polymer as a matrix and SWCNTs as reinforcement. From Fig. 2, the CNTs can be aligned as UD or functionally graded in the thickness direction of the polymer matrix.

The effective material properties of the FG-CNTRC plate are estimated by the rule of mixture [22]. Therefore, based on the modified rule of mixture, the effective material properties of the CNTRC plate are obtained as [4]:

$$E_{11} = \eta_1 V_{CNT} E_{11}^{CNT} + V_m E^m \quad \text{(a)}$$

$$\frac{\eta_2}{E_{22}} = \frac{V_{CNT}}{E_{22}^{CNT}} + \frac{V_m}{E^m} \quad \text{(b)} \qquad (1)$$

$$\frac{\eta_3}{G_{12}} = \frac{V_{CNT}}{G_{12}^{CNT}} + \frac{V_m}{G^m} \quad \text{(c)}$$

Where E_{11}^{CNT} and E_{22}^{CNT} are Young's moduli of CNTs in principle direction, and G_{12}^{CNT} indicates the shear modulus of CNTs. Also, E_{11}, E_{22} and G_{12} represent the effective elastic moduli and shear moduli of CNTs reinforced matrix, respectively. E^m and G^m are the Young's and shear moduli of the isotropic polymer matrix, respectively. Moreover $\eta_i \ (i = 1,2,3)$ are the CNT efficiency parameter where used to account for incompatibility in the load transfer between the nanotube and polymeric phases [23], V_m and V_{CNT} represent the volume fraction of matrix and CNTs of a unitary volume, respectively, and the relation between them is written as $V_m + V_{CNT} = 1$. The mass density of CNTRC plate is expressed as

$$\rho = V_{CNT}\ \rho^{CNT} + V_m\ \rho^m \qquad (2)$$

In which ρ^m and ρ^{CNT} indicate the densities of matrix and CNTs, respectively. Likewise, Poisson's ratio is written as

$$\nu_{12} = V_{CNT}^*\ \nu_{12}^{CNT} + V_m \nu^m,\ \nu_{21} = \nu_{12} E_{22} / E_{11} \qquad (3)$$

where ν_{12}^{CNT} and ν^m are the Poisson's ratio of CNTs and matrix, respectively, and V_{CNT}^* is obtained as [24]

$$V_{CNT}^* = \frac{\omega_{CNT}}{\omega_{CNT} + (\rho^{CNT} / \rho^m)(1 - \omega_{CNT})} \qquad (4)$$

In which, ω_{CNT} indicates the mass fraction of CNTs. The volume fractions of the five distribution types of CNTs in the polymer matrix are demonstrated as follows [20]

$$\text{UD}: \quad V_{CNT}(z) = V_{CNT}^* \quad \text{(a)}$$

$$\text{FG}-\text{A}: \quad V_{CNT}(z) = \left(1 - \frac{2z}{h}\right) V_{CNT}^* \quad \text{(b)}$$

$$\text{FG}-\text{V}: \quad V_{CNT}(z) = \left(1 + \frac{2z}{h}\right) V_{CNT}^* \quad \text{(c)} \qquad (5)$$

$$\text{FG}-\text{O}: \quad V_{CNT}(z) = 2\left(1 - \frac{2|z|}{h}\right) V_{CNT}^* \quad \text{(d)}$$

$$\text{FG}-\text{X}: \quad V_{CNT}(z) = \frac{4|z|}{h} V_{CNT}^* \quad \text{(e)}$$

2- 3- Kinetic relations

According to the classical plate theory, the displacement fields of an arbitrary point in the FG-CNTRC plates integrated with piezoelectric layers are written as

$$\begin{aligned} u_x &= u\left(x,y,t\right) - z\,\frac{\partial w}{\partial x}, \\ u_y &= v\left(x,y,t\right) - z\,\frac{\partial w}{\partial y}, \\ u_z &= w\left(x,y,t\right) \end{aligned} \tag{6}$$

Where u and v are in-plane displacements in x and y directions, respectively, and w is lateral displacement of points on the mid-plane of the plate. The linear strain-displacement relation for small deflection of the plate can be given as

$$\begin{aligned} \varepsilon_{xx} &= \frac{\partial u}{\partial x} - z\,\frac{\partial^2 w}{\partial x^2}, \\ \varepsilon_{yy} &= \frac{\partial v}{\partial y} - z\,\frac{\partial^2 w}{\partial y^2}, \\ \gamma_{xy} &= \frac{\partial u}{\partial y} + \frac{\partial v}{\partial x} - 2z\,\frac{\partial^2 w}{\partial x\,\partial y} \end{aligned} \tag{7}$$

2- 4- Electromechanical constitutive relations

Due to the orthotropic nature of CNTs, the stress-strain relationship of FG-CNTRC plates can be expressed as follows:

$$\begin{Bmatrix} \sigma_{xx} \\ \sigma_{yy} \\ \sigma_{xy} \end{Bmatrix} = \begin{bmatrix} Q_{11} & Q_{12} & 0 \\ Q_{12} & Q_{22} & 0 \\ 0 & 0 & Q_{66} \end{bmatrix} \left[\begin{Bmatrix} \varepsilon_{xx} \\ \varepsilon_{yy} \\ 2\varepsilon_{xy} \end{Bmatrix} \right] \tag{8}$$

Where,

$$\begin{aligned} Q_{11} &= \frac{E_{11}}{1-\nu_{12}\nu_{21}}, \quad Q_{12} = Q_{21} = \frac{\nu_{12}E_{22}}{1-\nu_{12}\nu_{21}}, \\ Q_{22} &= \frac{E_{22}}{1-\nu_{12}\nu_{21}}, \quad Q_{66} = G_{12} \end{aligned}$$

In which E_{11}, E_{22} are Young's moduli in the principle x and y directions, respectively, and G_{12} is the shear modulus in the $x-y$ plane, $\acute{\imath}_{12}$ and $\acute{\imath}_{21}$ are the Poisson's ratio. In addition, the constitutive relation of transversely isotropic piezoelectric layers is given as [25]

$$\begin{Bmatrix} \sigma_{xx} \\ \sigma_{yy} \\ \sigma_{xy} \end{Bmatrix} = \begin{bmatrix} \bar{C}'_{11} & \bar{C}'_{12} & 0 \\ \bar{C}'_{12} & \bar{C}'_{11} & 0 \\ 0 & 0 & 1/2\left(\bar{C}'_{11}-\bar{C}'_{12}\right) \end{bmatrix} \begin{Bmatrix} \varepsilon_{xx} \\ \varepsilon_{yy} \\ 2\varepsilon_{xy} \end{Bmatrix} - \begin{bmatrix} 0 & 0 & \bar{e}_{31} \\ 0 & 0 & \bar{e}_{31} \\ 0 & 0 & 0 \end{bmatrix} \begin{Bmatrix} E_x \\ E_y \\ E_z \end{Bmatrix} \tag{9}$$

$$\begin{Bmatrix} D_x \\ D_y \\ D_z \end{Bmatrix} = \begin{bmatrix} 0 & 0 & 0 \\ 0 & 0 & 0 \\ \bar{e}_{31} & \bar{e}_{31} & 0 \end{bmatrix} \begin{Bmatrix} \varepsilon_{xx} \\ \varepsilon_{yy} \\ 2\varepsilon_{xy} \end{Bmatrix} - \begin{bmatrix} \Xi_{11} & 0 & 0 \\ 0 & \Xi_{11} & 0 \\ 0 & 0 & \bar{\Xi}_{33} \end{bmatrix} \begin{Bmatrix} E_x \\ E_y \\ E_z \end{Bmatrix} \tag{10}$$

In which,

$$\begin{aligned} \bar{C}'_{11} &= C_{11} - \frac{C_{13}^2}{C_{33}}, \quad \bar{C}'_{12} = C_{12} - \frac{C_{13}^2}{C_{33}}, \\ \bar{e}_{31} &= e_{31} - \frac{C_{13}}{C_{33}} e_{33}, \quad \bar{\Xi}_{33} = \Xi_{33} - \frac{e_{33}^2}{C_{33}} \end{aligned}$$

Where E_i and D_i $(i = x, y, z)$ are the electric field and electric displacement in the piezoelectric layer, respectively. Also, C_{ij}, e_{ij} and Ξ_{ij} $(i, j = 1,2,3)$ represent the piezoelectric elastic moduli, piezoelectric constant, and dielectric permittivity, respectively. The electric field is written in terms of electric potential as:

$$E_x = -\frac{\partial \Phi}{\partial x}, \; E_y = -\frac{\partial \Phi}{\partial y}, \; E_z = -\frac{\partial \Phi}{\partial z} \tag{11}$$

Where Φ indicates the electric potential of the piezoelectric layer in the thickness direction. Here, two common types of an open and closed circuits of piezoelectric layers are considered. For pure piezoelectric plates, Lee and

Lin [26] presented a sinusoidal variation of electric potential in the thickness direction for the case when electrodes are shortly connected. But for piezoelectric coupled plates a quadratic function is used for both open and closed circuit conditions. This quadratic variation of the electric potential in the lateral direction was investigated by Wang et al. [9, 27]. When both sides major surface of the piezoelectric layers are held at zero voltage (closed circuit), the variation of electric potential represents as [27]:

$$\Phi(x,y,z,t)=\begin{cases}\phi(x,y,t)\left[1-\left(\dfrac{z-\frac{h}{2}-\frac{h_p}{2}}{\frac{h_p}{2}}\right)^2\right], \\ \dfrac{h}{2}\le z\le\dfrac{h}{2}+h_p \\ \phi(x,y,t)\left[1-\left(\dfrac{-z-\frac{h}{2}-\frac{h_p}{2}}{\frac{h_p}{2}}\right)^2\right], \\ -\dfrac{h}{2}-h_p\le z\le-\dfrac{h}{2}\end{cases} \tag{12}$$

Where ϕ indicates the electric potential in the neutral surface of the piezoelectric layer. When the outer major surface of piezoelectric layers is exposed to a low-permeability environment such as vacuum or airflow, the environment is performed as an electric insulation. Therefore, the electric displacement vector (D_z) in the perpendicular outer surface of the piezoelectric layer will be zero, while the inner surface of the piezoelectric layer (piezoelectric layer and CNTRC plate interface) is short-circuited. The electric potential for open circuit condition is defined below [9]:

$$\Phi(x,y,z,t)=\begin{cases}\phi(x,y,t)\left[1-\left(\dfrac{z-\frac{h}{2}-\frac{h_p}{2}}{\frac{h_p}{2}}\right)^2+\dfrac{4(z-h)}{h_p}\right] \\ +\dfrac{\bar{e}_{31}}{\bar{\Xi}_{33}}\left[\left(\dfrac{\partial u}{\partial x}+\dfrac{\partial v}{\partial y}\right)-\left(\dfrac{\partial^2 w}{\partial x^2}+\dfrac{\partial^2 w}{\partial y^2}\right)(h+h_p)\right](z-h), \\ \dfrac{h}{2}\le z\le\dfrac{h}{2}+h_p \\ \phi(x,y,t)\left[1-\left(\dfrac{-z-\frac{h}{2}-\frac{h_p}{2}}{\frac{h_p}{2}}\right)^2-\dfrac{4(z+h)}{h_p}\right] \\ +\dfrac{\bar{e}_{31}}{\bar{\Xi}_{33}}\left[\left(\dfrac{\partial u}{\partial x}+\dfrac{\partial v}{\partial y}\right)+\left(\dfrac{\partial^2 w}{\partial x^2}+\dfrac{\partial^2 w}{\partial y^2}\right)(h+h_p)\right](z+h), \\ -\dfrac{h}{2}-h_p\le z\le-\dfrac{h}{2}\end{cases} \tag{13}$$

2- 5- Modeling of solid-flow interaction

In this study, the first-order piston theory is applied for the modeling of solid-flow interactions as follows [28]:

$$\Delta P=-\frac{\rho_\infty U_\infty^2}{\sqrt{M_\infty^2-1}}\left(\frac{\partial w}{\partial x}+\frac{M_\infty^2-2}{M_\infty^2-1}\frac{1}{U_\infty}\frac{\partial w}{\partial t}\right) \tag{14}$$

Where U_∞, M_∞ and ρ_∞ indicate velocity, Mach number, and density of airflow in the outer fluid boundary layer, respectively.

3- Governing Equations

Based on the extended Hamilton's variation principle, the following governing equations of FG-CNTRC plates with piezoelectric layers are obtained as:

$$\frac{\partial N_{xx}}{\partial x}+\frac{\partial N_{xy}}{\partial y}=I_0\frac{\partial^2 u}{\partial t^2}-I_1\frac{\partial^3 w}{\partial x\,\partial t^2} \tag{a}$$

$$\frac{\partial N_{xy}}{\partial x}+\frac{\partial N_{yy}}{\partial y}=I_0\frac{\partial^2 v}{\partial t^2}-I_1\frac{\partial^3 w}{\partial y\,\partial t^2} \tag{b}$$

$$\begin{aligned}&\frac{\partial^2 M_{xx}}{\partial x^2}+\frac{\partial^2 M_{yy}}{\partial y^2}+2\frac{\partial^2 M_{xx}}{\partial x\,\partial y}+\\ &R_{xx}\frac{\partial^2 w}{\partial x^2}+R_{yy}\frac{\partial^2 w}{\partial y^2}+\Delta P=I_0\frac{\partial^2 w}{\partial t^2}+\\ &I_1\left(\frac{\partial^3 u}{\partial x\,\partial t^2}+\frac{\partial^3 v}{\partial y\,\partial t^2}\right)-I_2\left(\frac{\partial^4 w}{\partial x^2\partial t^2}+\frac{\partial^4 w}{\partial y^2\partial t^2}\right)\end{aligned} \tag{c}$$

(15)

Where ΔP is the supersonic airflow pressure. Also, I_0, I_1 and I_2 indicate the rotary inertial coefficient, and expressed as

$$(I_0,I_1,I_2)=\int_{-\frac{h}{2}-h_p}^{\frac{h}{2}+h_p}\rho(1,z,z^2)dz \tag{16}$$

Moreover, stress resultants N_{ij}, M_{ij} $(i,j=x,y)$ are expressed as

$$\begin{aligned}&N_{xx},N_{xy},N_{yy},M_{xx},M_{xy},M_{yy}=\\ &\int_{-\frac{h}{2}-h_p}^{\frac{h}{2}+h_p}(\sigma_{xx},\sigma_{xy},\sigma_{yy},\sigma_{xx}z,\sigma_{xy}z,\sigma_{yy}z)dz\end{aligned} \tag{17}$$

Substituting the stress resultant (Eq. (17)) into Eqs. (15), the governing differential equations in terms of displacement fields can be achieved as

$$\left(A_1+A_{11}^{'}\right)\frac{\partial^2 u}{\partial x^2}+\left(C_1+A_{66}^{'}\right)\frac{\partial^2 u}{\partial y^2}+$$
$$\left(\nu_{12}B_1+A_{12}^{'}+C_1+A_{66}^{'}\right)\frac{\partial^2 v}{\partial x\,\partial y}-$$
$$\left(\nu_{12}B_2+2C_2\right)\frac{\partial^3 w}{\partial x\,\partial y^2}-A_2\frac{\partial^3 w}{\partial x^3}= \quad \text{(a)}$$
$$I_0\frac{\partial^2 u}{\partial t^2}-I_1\frac{\partial^3 w}{\partial x\,\partial t^2}$$
$$\left(B_1+A_{11}^{'}\right)\frac{\partial^2 v}{\partial y^2}+\left(C_1+A_{66}^{'}\right)\frac{\partial^2 v}{\partial x^2}+$$
$$\left(\nu_{12}B_1+A_{12}^{'}+C_1+A_{66}^{'}\right)\frac{\partial^2 u}{\partial x\,\partial y}-$$
$$\left(\nu_{12}B_2+2C_2\right)\frac{\partial^3 w}{\partial y\,\partial x^2}-B_2\frac{\partial^3 w}{\partial y^3}= \quad \text{(b)}$$
$$I_0\frac{\partial^2 v}{\partial t^2}-I_1\frac{\partial^3 w}{\partial y\,\partial t^2} \quad (18)$$
$$-\left(A_3+D_{11}^{'}\right)\frac{\partial^4 w}{\partial x^4}-$$
$$\left(2\nu_{12}B_3+D_{12}^{'}+D_{11}^{'}+4D_{66}^{'}+4C_3\right)\frac{\partial^4 w}{\partial x^2\partial y^2}-$$
$$\left(B_3+D_{12}^{'}\right)\frac{\partial^4 w}{\partial y^4}+A_2\frac{\partial^3 u}{\partial x^3}+B_2\frac{\partial^3 v}{\partial y^3}+$$
$$\left(2C_2+\nu_{12}B_2\right)\left(\frac{\partial^3 v}{\partial x^2\partial y}+\frac{\partial^3 u}{\partial x\,\partial y^2}\right)+$$
$$R_{xx}\frac{\partial^2 w}{\partial x^2}+R_{yy}\frac{\partial^2 w}{\partial y^2}-\zeta_1\left(\frac{\partial^2\phi}{\partial x^2}+\frac{\partial^4\phi}{\partial y^2}\right)+\Delta P= \quad \text{(c)}$$
$$I_0\frac{\partial^2 w}{\partial t^2}+I_1\left(\frac{\partial^3 u}{\partial x\,\partial t^2}+\frac{\partial^3 v}{\partial y\,\partial t^2}\right)-$$
$$I_2\left(\frac{\partial^4 w}{\partial x^2\partial t^2}+\frac{\partial^4 w}{\partial y^2\partial t^2}\right)$$

The coefficients in Eqs. (18) are given in Appendix A. The mechanical edge boundary conditions are fully movable simply supported (SSSS). In this regard, the mathematical implementation of these edge boundary conditions can be expressed as

$$N_{xx}=N_{xy}=w=M_{xx}=M_{xy}=0;\quad \text{at } x=0 \text{ and } x=a \quad (19)$$
$$N_{yy}=N_{xy}=w=M_{yy}=M_{xy}=0;\quad \text{at } y=0 \text{ and } y=b$$

3- 1- Maxwell equation

Noted that all of the electrical variables must satisfy the Maxwell equation, which requires the following integration across the thickness of the piezoelectric layers to be zero for any x and y as [10]

$$\int_{\frac{h}{2}}^{\frac{h}{2}+h_p}\left(\frac{\partial D_x}{\partial x}+\frac{\partial D_y}{\partial y}+\frac{\partial D_z}{\partial z}\right)dz+\int_{-\frac{h}{2}-h_p}^{-\frac{h}{2}}\left(\frac{\partial D_x}{\partial x}+\frac{\partial D_y}{\partial y}+\frac{\partial D_z}{\partial z}\right)dz=0 \quad (20)$$

Substituting Eq. (10) in conjunction with Eqs. (7) and (11) into above Maxwell's equation and simplifying the result gives

$$-\mu_1\left(\frac{\partial^2\phi}{\partial x^2}+\frac{\partial^2\phi}{\partial y^2}\right)+\mu_2\left(\frac{\partial^4 w}{\partial x^4}+2\frac{\partial^4 w}{\partial x^2\partial y^2}+\frac{\partial^4 w}{\partial y^4}\right)-\mu_3\left(\frac{\partial^2 w}{\partial x^2}+\frac{\partial^2 w}{\partial y^2}\right)+\mu_4\phi=0 \quad (21)$$

This equation shows the coupling between mechanical and electrical effects. For the open and closed circuit conditions, coefficients $\mu_1,\ldots,\mu_4$ are depicted in Appendix A. The boundary condition for ϕ in both closed and open circuits is considered as follows [10]

$$\phi(x=0,a;y)=\phi(x;y=0,b)=0 \quad (22)$$

3- 2- Dimensionless form of the governing equations

In order to parametric study, the following non-dimensional parameter is utilized,

$$\xi=\frac{x}{a},\eta=\frac{y}{b},r=\frac{a}{b},H=\frac{h}{a},$$
$$H_p=\frac{h_p}{h},\tau=t\sqrt{\frac{D_0}{\rho_m h a^4}},$$
$$r_{xx}=-\frac{R_{xx\,a^2}}{\left(A_3+D_{11}^{'}\right)},r_{yy}=-\frac{R_{yy\,a^2}}{\left(A_3+D_{11}^{'}\right)}, \quad (23)$$
$$\lambda=\frac{\rho_\infty U_\infty^2 a^3}{\left(A_3+D_{11}^{'}\right)\sqrt{M_\infty^2-1}},\mu=\frac{\rho_\infty a}{\rho_m h}$$

Where $D_0 = \frac{E_m}{12\left(1-\nu_m^2\right)}$ is the flexural rigidity of the polymer matrix. Herein, for a high Mach number, the following simplification is applied [29],

$$\frac{M_\infty^2-2}{M_\infty^2-1}\left(\frac{\mu}{\lambda\sqrt{M_\infty^2-1}}\right)^{1/2}=\left(\frac{\mu}{\lambda M_\infty}\right)^{1/2} \tag{24}$$

4- Solution Procedure

Galerkin's approach is applied to solve the governing equations. In this technique, the displacement fields may be expressed as a function of linear combinations of a finite number of proper shape functions with time-dependent vectors as follows

$$\begin{aligned} u\left(\xi,\eta,\tau\right)&=\boldsymbol{\Psi}_{\mathbf{u}}^{\mathbf{T}}\left(\xi,\eta\right)\mathbf{q}_{\mathbf{u}}\left(\tau\right),\\ v\left(\xi,\eta,\tau\right)&=\boldsymbol{\Psi}_{\mathbf{v}}^{\mathbf{T}}\left(\xi,\eta\right)\mathbf{q}_{\mathbf{v}}\left(\tau\right)\\ w\left(\xi,\eta,\tau\right)&=\boldsymbol{\Psi}_{\mathbf{w}}^{\mathbf{T}}\left(\xi,\eta\right)\boldsymbol{q}_{w}\left(\tau\right),\\ \phi\left(\xi,\eta,\tau\right)&=\boldsymbol{\Psi}_{\phi}^{\mathbf{T}}\left(\xi,\eta\right)\mathbf{q}_{\phi}\left(\tau\right) \end{aligned} \tag{25}$$

In which $\boldsymbol{\Phi}_{\mathbf{u}}$, $\boldsymbol{\Phi}_{\mathbf{v}}$, $\boldsymbol{\Phi}_{\mathbf{w}}$ and $\boldsymbol{\Phi}_{\phi}$ are the shape functions and $\mathbf{q}_{\mathbf{u}}$, $\mathbf{q}_{\mathbf{v}}$, $\mathbf{q}_{\mathbf{w}}$ and $\mathbf{q}_{\phi}$ are the time-dependent vectors of generalizing coordinates. The shape function must be chosen so that satisfies both the mechanical and electrical boundary conditions. Therefore, based on the boundary condition (Eqs. (19) and (22)) the shape functions for fully movable simply supported edge boundary conditions can be written as

$$\begin{aligned} \boldsymbol{\Psi}_{\mathbf{u}}\left(\xi,\eta\right)&=\sum_{i=1}^{M}\sum_{j=1}^{N}\cos(i\,\pi\xi)sin\left(j\,\pi\eta\right),\\ \boldsymbol{\Psi}_{\mathbf{v}}\left(\xi,\eta\right)&=\sum_{i=1}^{M}\sum_{j=1}^{N}\sin(i\,\pi\xi)cos\left(j\,\pi\eta\right)\\ \boldsymbol{\Psi}_{\mathbf{w}}\left(\xi,\eta\right)&=\sum_{i=1}^{M}\sum_{j=1}^{N}\sin(i\,\pi\xi)sin\left(j\,\pi\eta\right),\\ \boldsymbol{\Psi}_{\phi}\left(\xi,\eta\right)&=\sum_{i=1}^{M}\sum_{j=1}^{N}\sin(i\,\pi\xi)sin\left(j\,\pi\eta\right) \end{aligned} \tag{26}$$

Substituting approximate displacement expressions (Eq. (26) into Eqs. (18) and (21), multiplying both sides of the equations by shape functions and integrating over the whole region, the discretized expressions for the equations of motion are obtained as

$$\left[\mathbf{M}\right]\ddot{\mathbf{q}}\left(\boldsymbol{\tau}\right)+\left[\mathbf{C}\right]\dot{\mathbf{q}}\left(\boldsymbol{\tau}\right)+\left[\mathbf{K}_{\mathbf{e}}\right]\mathbf{q}\left(\boldsymbol{\tau}\right)=\mathbf{0} \tag{27}$$

Where $\mathbf{q}=\left\{\mathbf{q}_{\mathbf{u}}\,,\mathbf{q}_{\mathbf{v}}\,,\mathbf{q}_{\mathbf{w}}\right\}$ is the overall vector of generalized coordinates and $\mathbf{M}$, $\mathbf{C}$ and $\mathbf{K}_{\mathbf{e}}$ are the mass matrix, damping matrix, and reduced stiffness matrix of the system, respectively. Therefore, the stiffness matrix is expressed as

$$\begin{bmatrix}\mathbf{K_{11}} & \mathbf{K_{12}} & \mathbf{K_{13}} & \mathbf{K_{14}}\\ \mathbf{K_{21}} & \mathbf{K_{22}} & \mathbf{K_{23}} & \mathbf{K_{24}}\\ \mathbf{K_{31}} & \mathbf{K_{32}} & \mathbf{K_{33}} & \mathbf{K_{34}}\\ \mathbf{K_{41}} & \mathbf{K_{42}} & \mathbf{K_{43}} & \mathbf{K_{44}}\end{bmatrix}\begin{Bmatrix}\mathbf{q_u}\\ \mathbf{q_v}\\ \mathbf{q_w}\\ \mathbf{q}_{\phi}\end{Bmatrix}=\mathbf{0} \tag{28}$$

The above equation can be rewritten as:

$$\begin{aligned} \bar{\mathbf{K}}_{\mathbf{11}}\mathbf{q}+\bar{\mathbf{K}}_{\mathbf{12}}\mathbf{q}_{\phi}&=\mathbf{0},\\ \bar{\mathbf{K}}_{\mathbf{21}}\mathbf{q}+\mathbf{K_{44}}\mathbf{q}_{\phi}&=\mathbf{0} \end{aligned} \tag{29}$$

Where,

$$\bar{\boldsymbol{K}}_{11}=\begin{bmatrix}\mathbf{K_{11}} & \mathbf{K_{12}} & \mathbf{K_{13}}\\ \mathbf{K_{21}} & \mathbf{K_{22}} & \mathbf{K_{23}}\\ \mathbf{K_{31}} & \mathbf{K_{32}} & \mathbf{K_{33}}\end{bmatrix},$$

$$\mathbf{q}=\left\{\mathbf{q}_{\mathbf{u}}\ \mathbf{q}_{\mathbf{v}}\ \mathbf{q}_{\mathbf{w}}\right\}^{\mathrm{T}},$$

$$\bar{\mathbf{K}}_{\mathbf{12}}=\begin{bmatrix}\mathbf{K_{14}} & \mathbf{K_{24}} & \mathbf{K_{34}}\end{bmatrix}^{\mathrm{T}}$$

$$\bar{\mathbf{K}}_{\mathbf{21}}=\begin{bmatrix}\mathbf{K_{41}} & \mathbf{K_{42}} & \mathbf{K_{43}}\end{bmatrix}$$

Then, from Eq. (29), the reduced stiffness matrix is obtained as follows

$$\mathbf{K_e}=\bar{\mathbf{K}}_{\mathbf{11}}-\bar{\mathbf{K}}_{\mathbf{12}}\,\mathbf{K}_{\mathbf{44}}^{-\mathbf{1}}\,\bar{\mathbf{K}}_{\mathbf{21}} \tag{30}$$

4- 1- Dynamic Stability analysis

In order for dynamic stability analysis, Eq. (27) is transformed into first-order state-space form as below [30]

$$\dot{\mathbf{Z}}\left(\tau\right)=\left[\mathbf{A}\right]\mathbf{Z}\left(\tau\right) \tag{31}$$

Where the state vector $\mathbf{Z}\left(\tau\right)$ and state matrix $[\mathbf{A}]$ is defined as

$$\begin{aligned} \mathbf{Z}\left(\tau\right)&=\left\{\mathbf{q}\,,\dot{\mathbf{q}}\right\}^{T},\\ \left[\mathbf{A}\right]&=\begin{bmatrix}\left[\mathbf{0}\right] & \left[\mathbf{I}\right]\\ -\left[\mathbf{M}\right]^{-1}\left[\mathbf{K_e}\right] & -\left[\mathbf{M}\right]^{-1}\left[\mathbf{C}\right]\end{bmatrix} \end{aligned} \tag{32}$$

In which $[\mathbf{I}]$ indicates the unitary matrix. To solve the first-order, linear ordinary differential equation (Eq. (31)), the simple exponential function of time can be considered

$$\mathbf{Z}(\tau)=\mathbf{X}exp(\Omega\tau) \tag{33}$$

Where Ω and $\mathbf{X}$ indicate complex eigenvalue and corresponding eigenvector, respectively. Substitution of this expression into (Eq. 31) a standard eigenvalue problem is achieved as follows

$$([\mathbf{A}]-\Omega[\mathbf{I}])\mathbf{Z}(\tau)=0 \tag{34}$$

Since the system is non-conservative, the eigenvalues are complex quantities in general, i.e. $\Omega=Re(\Omega)\pm iIm(\Omega)$. It should be noted that the real and imaginary parts of complex eigenvalue indicate damping effects and natural frequency of the dynamic system, respectively. The dynamic stability region is specified owing to the sign of the real part of the complex eigenvalue [31, 32].

4- 2- Static stability analysis

In static stability analysis, the derivative with respect to time is neglected. Therefore, Eq. (27) is reduced as

$$[\mathbf{K}_e]\mathbf{q}=0 \tag{35}$$

For a nontrivial solution of the generalized coordinate deflection, the determinant of $\mathbf{K}_e$ should be zero. Therefore,

$$\det[\mathbf{K}_e]=0 \tag{36}$$

Solving the above equation in terms of non-dimensional in-plane force, the critical in-plane force is obtained. In this state, the imaginary part of the complex eigenvalue frequency is equal to zero, and the static stability region is known according to the sign of the real part of the complex eigenvalue.

5- Numerical Results and Discussion

In this section, the parametric study on the aero-elastic characteristics of FG-CNTRC plates integrated with identical piezoelectric layers on both top and bottom surfaces is taken into account. In all numerical analyses, ten-mode numbers have been considered. Unless otherwise mentioned, it is assumed the FG-CNTRC plates are fully covered by the PZT-4 piezoelectric layer; and the length-to-thickness ratio is supposed to be 0.01 ($h/a=0.01$), length to width ratio is equal to 1 ($r=1$, square plate) and $\mu/M_\infty=0.1$. Polymethyl-methacrylate (PMMA) is considered as the polymer matrix, and SWCNTs (10,10) are selected as a reinforcement. Herein the effects of the piezoelectric layers, CNTs distribution, and volume fraction on the static and dynamic stability boundaries are investigated in detail. The material properties of CNT and polymer matrix are taken as [33]:

$$\begin{aligned}
&E^m=2.5\,\text{Gpa},\ \ \rho^m=1150\,\text{Kg/m}^3,\\
&E_{11}^{CNT}=5.6466\,\text{Tpa},\ \ \nu_{12}^{CNT}=0.175\\
&E_{22}^{CNT}=7.08\,\text{Tpa},\\
&G_{12}^{CNT}=1.9445\,\text{Tpa},\ \ \rho^{CNT}=1400\,\text{Kg/m}^3
\end{aligned}$$

As reported by Han and Elliott [34], the CNT efficiency parameter is an essential key in the rule of mixture for determining the effective mechanical properties of the nanocomposite. Therefore, to modify the rule of mixture, the CNT efficiency parameter is achieved by matching the mechanical properties obtained by the Molecular Dynamic (MD) simulation and those calculated from the rule of mixture. The value of the CNT efficiency parameter can be considered as Ref. [33]. In this study, the numerical result for different kinds of piezoelectric material properties is evaluated. The values of piezoelectric material parameters are depicted in Ref. [35].

To check the validity of the present formulation, the result of this study is compared with the available result in the reported literature. In the first case study, the dynamic stability boundary of an isotropic square plate ($r=1$) is determined and compared with the results reported by Dugundgi [36]. In this analytical investigation, Dugundgi considered the rectangular plate has structural damping and simply supported on all four edges (SSSS). Variation of the critical aerodynamic pressure versus total structural damping is depicted in Fig. 3. The result reveals a good agreement between the present formulation and the result in Ref. [36].

The second comparative study is dedicated to close circuit resonant frequencies of an FGM plate which is fully covered by identical piezoelectric layers on both top and bottom surfaces. Table 1 shows the presently computed non-dimensional natural frequencies ($\bar{\beta}=\omega\pi^2(a/h)\sqrt{\rho_m/E_m}$) with those reported by Hasani Baferani et al. [37], for the piezoelectric thickness ratio $H_p=h_p/h$ descending from 0.1 to 0. It is seen that the resonant frequency of the FGM plate integrated with piezoelectric layers approaches that for the FGM plate without piezoelectric layers as the piezoelectric thickness ratio approaches zero for closed circuit condition.

Variations of the critical aerodynamic pressure and the critical frequency of FG-CNTRC plates versus the non-dimensional piezoelectric thickness H_p are depicted in Fig. 4(a) and (b), respectively. In this figure, both open and closed circuit conditions are considered and the other remaining parameters are constant at $V_{CNT}^*=0.12$, $r_{xx}=r_{yy}=0$. It can be seen from Fig. 4(a) and (b), by increasing the non-dimensional piezoelectric thickness, both critical aerodynamic pressure and critical frequency increase smoothly. Thus, the

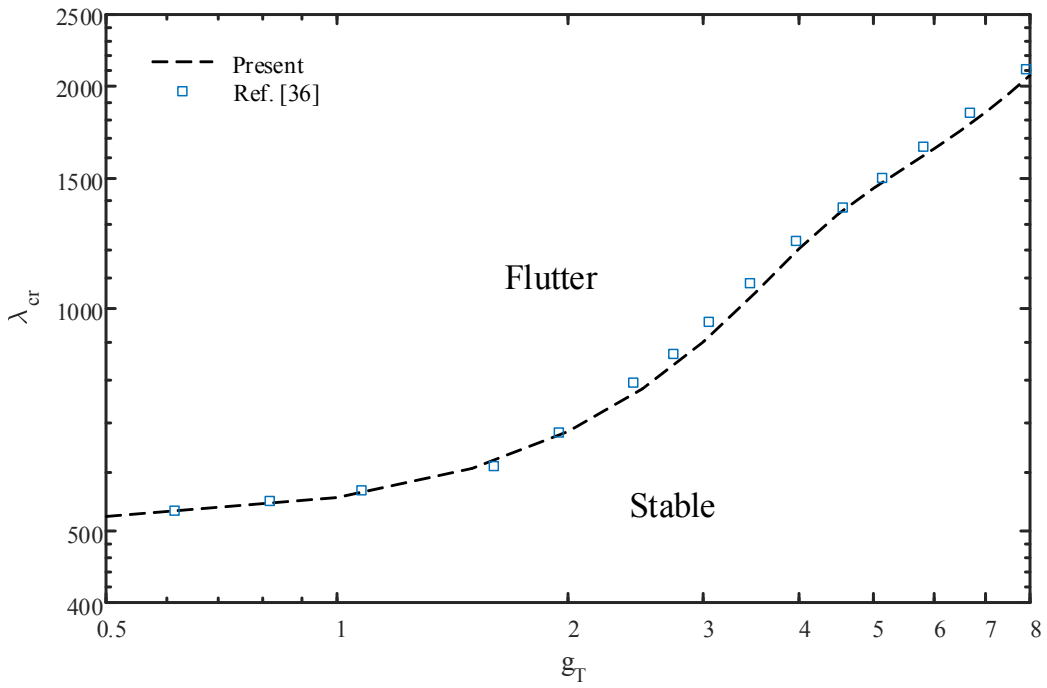

Fig. 3. Comparison of non-dimensional critical aerodynamic pressure for an isotropic square plate

Table 1. Comparison between the result of the present model with those given by Hasani Baferani et al. [37] for square simply supported FGM plate in closed circuit condition

Power index	h_p / h	method	1st	2nd	3rd
0.5	10^{-1}	present	90.9301	227.0753	362.9216
	10^{-2}		97.0020	242.3683	387.5710
	10^{-4}		98.1228	245.1840	392.0977
	0		98.1347	245.2139	392.1459
		Ref. [37]	98.0136	245.3251	392.4425
	Discrepancy (%)		0.12	0.04	0.07
1	10^{-1}	present	83.7493	209.1161	334.1756
	10^{-2}		87.5887	218.8385	349.9285
	10^{-4}		88.4175	220.9257	353.2928
	0		88.4264	220.9482	353.3290
		Ref. [37]	88.3093	221.0643	353.6252
	Discrepancy (%)		0.13	0.05	0.08

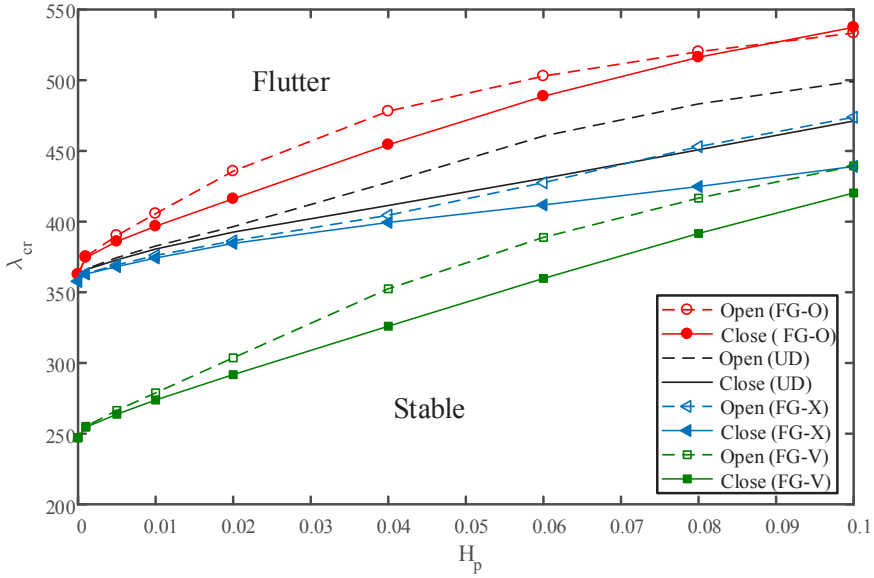

a)

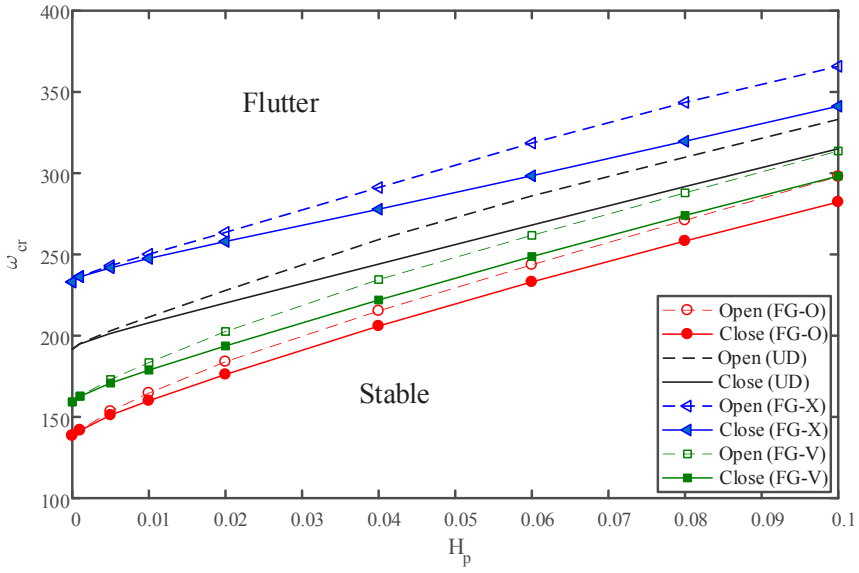

b)

Fig. 4. Influence of non-dimensional piezoelectric thickness on the dynamic stability of various FG-CNTRC plates in close and open circuit conditions of piezoelectric layers; (a) Non-dimensional critical aerodynamic pressure and (b) Non-dimensional critical frequency.

flutter occurred at a higher aerodynamic pressure and higher critical frequency. This means that the influence of flexural rigidity of piezoelectric layers dominates the effect of their mass density [38]. It is inferred from Fig. 4(a) that, the FG-O plate and FG-V plate have the highest and lowest dynamic stable region, respectively. Because, the strengthening of stiffness near the mid-plane of the FG-CNTRC plate is more effective in rising the aero-elastic stability [12, 21]. Though, Fig. 4(b) shows that the maximum and minimum values of critical frequency belong to the FG-X plate and FG-O plate, respectively. This is because, for FG-X distribution of CNTs, the plate will be stiffer in bending mode vibration; thus the critical frequency increased [5]. It may be further concluded that the critical aerodynamic pressure and the critical frequency in the state of the open circuit condition are higher than in the closed circuit condition. Because, in open circuit boundary condition the electric potential transforms to mechanical energy during vibration, while closed-circuit discharges the electric potential [39].

The effect of the different CNT volume fractions (V_{CNT}^{*}) on the FG-V plate is shown in Fig. 5. In this figure, both open and closed circuit conditions are considered and the other parameters are fixed as $r_{xx} = r_{yy} = 0$. It can be seen from Fig. 5(a), by increasing the CNT volume fraction, the stable region decreases as long as increasing the non-dimensional piezoelectric thickness. Though, Fig. 5(b) shows that by increasing the CNT volume fraction, the critical frequency rises as long as increasing the non-dimensional piezoelectric thickness; because the plate will be stiffer.

The effect of the material piezoelectric layer on the critical aerodynamic pressure and critical frequency of the FG-V plate for close circuit conditions are depicted in Fig. 6(a) and (b). In this figure, the parameters are fixed at $V_{CNT}^{*} = 0.12$, $r_{xx} = r_{yy} = 0$. The results show that material piezoelectric layer PZT-6B and PZT-5H gives the largest and lowest dynamic stable region.

Fig. 7(a) and (b), represent the variation of critical aerodynamic pressure of a UD plate enclosed by piezoelectric layers against non-dimensional in-plane forces in x and y direction, respectively. In Fig 7(a) the parameters have the value of $H_p = 0.05$, $r_{yy} = 0$ and $V_{CNT}^{*} = 0.12$. It can be observed that, by increasing the non-dimensional in-plane force in x direction, the critical aerodynamic pressure decreases. Because the stiffness of the plate decreases by applying the compressive in-plane force in x direction [20]. Also, the critical aerodynamic pressure is raised by the enhancement of non-dimensional piezoelectric thickness. The influence of non-dimensional in-plane force in y direction on the critical aerodynamic pressure is depicted in Fig. 7(b). In this figure the parameters are fixed at $H_p = 0.05$, $r_{xx} = 0$ and $V_{CNT}^{*} = 0.12$. It is realized that the UD plate integrated with piezoelectric layers gives a larger stable region compared to a plate without piezoelectric layers.

Fig. 8(a) and (b) indicate the variation of the non-dimensional critical in-plane force versus the non-dimensional piezoelectric thickness in x and y direction, respectively. The FG-CNTRC plate enclosed by piezoelectric layers in open and closed circuit conditions are considered. In Fig. 8(a), the parameters have the value as $\lambda = 0$, $r_{yy} = 0$ and $V_{CNT}^{*} = 0.12$. The results show that, with the increase of non-dimensional piezoelectric thickness, the critical non-dimensional in-plane force in x direction increases. With regard to present non-dimensionalization, the FG-O plate gives the largest static stability region with respect to the other plate. The critical non-dimensional in-plane force in open circuit condition is larger than the closed circuit condition as mentioned before. Fig. 8(b) indicates the variation of critical non-dimensional in-plane force in y direction versus non-dimensional piezoelectric thickness. In this figure the parameters are fixed at $\lambda = 0$, $r_{yy} = 0$ and $V_{CNT}^{*} = 0.12$. It is observed that by increasing the non-dimensional piezoelectric thickness, the critical non-dimensional in-plane force in y direction (r_{yy}) increases. According to the present non-dimensionalization, the results exhibited that the FG-O plate gives the largest static stability region compared to the other plates.

The effect of aerodynamic pressure on the static stability (divergence) region of the UD plate is depicted in Fig. 9. It can be observed that the static stability region is increased by the enhancement of the non-dimensional aerodynamic pressure.

6- Concluding Remarks

In this study, the stability analysis of FG-CNTRC plates with surfaces fully covered by two identical piezoelectric layers subjected to supersonic airflow was studied based on Kirchhoff's plate theory. The aerodynamic force exerted on the top surface of the hybrid plate was simulated by employing first-order piston theory. The mechanical and electrostatic governing equations were obtained by using Hamilton's variation principle and Maxwell's equation, respectively. It was assumed the hybrid plate is movable simply supported on all four edges. Variation of the electric potential across the piezoelectric thickness was described by using a combination of linear and quadratic functions. The close and open circuit conditions were considered for the top and bottom surfaces of piezoelectric layers. The coupled electromechanical governing equations were discretized by applying Galerkin's approach. The obtained results from this formulation were evaluated with available data in the literature. To analyze the aero-elastic behavior, the influence of non-dimensional piezoelectric thickness, kinds of piezoelectric materials, electric boundary conditions of piezoelectric layers, CNT volume fraction, and CNTs distribution patterns in the polymer matrix on the stability boundaries were investigated. The following main conclusion can be remarked:

By increasing non-dimensional piezoelectric thickness, the critical aerodynamic pressure and critical frequency are increased.

The aero-elastic behavior of both the FG-V plate and the FG-A plate are exactly identical to each other.

Our results show that the FG-O plate and FG-V plate include the largest and smallest critical aerodynamic pressure, respectively.

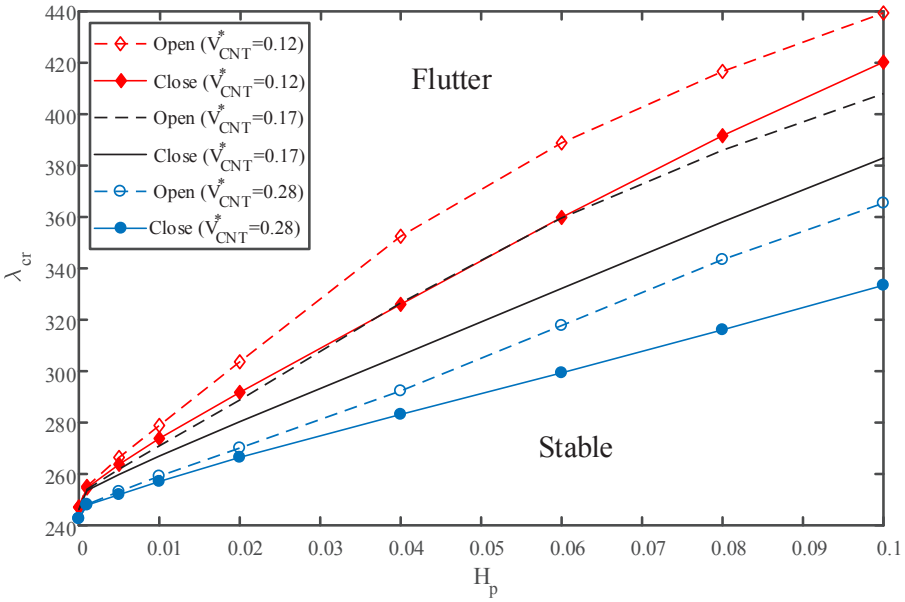

a)

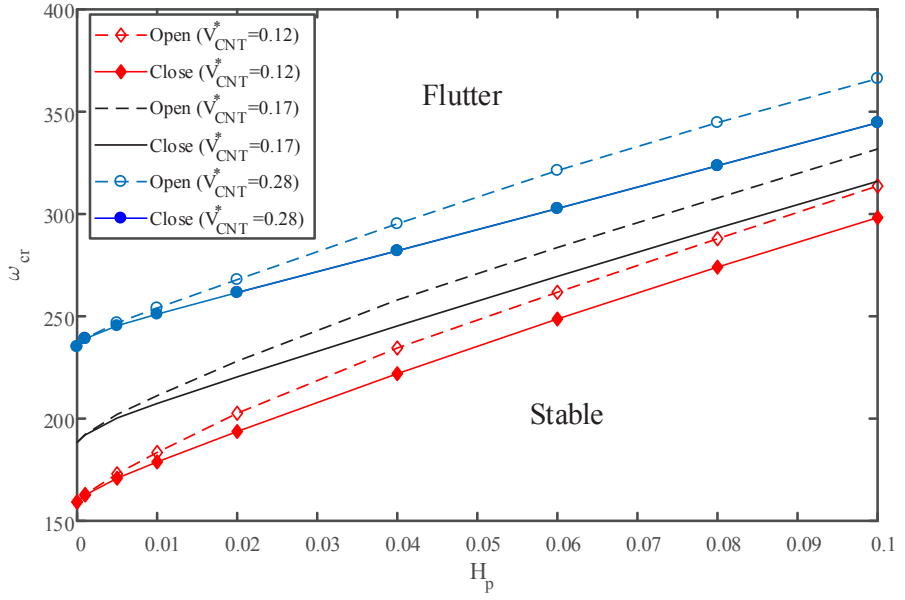

b)

Fig. 5. Variation of (a) Non-dimensional critical aerodynamic pressure and (b) Non-dimensional critical frequency of FG-V plate versus the non-dimensional piezoelectric thickness for three values of V^*_{CNT} .

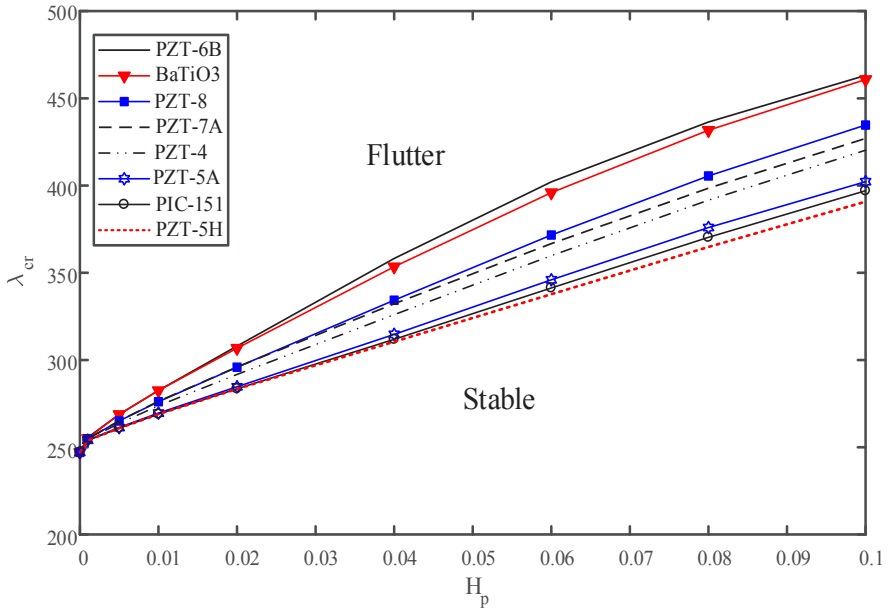

a)

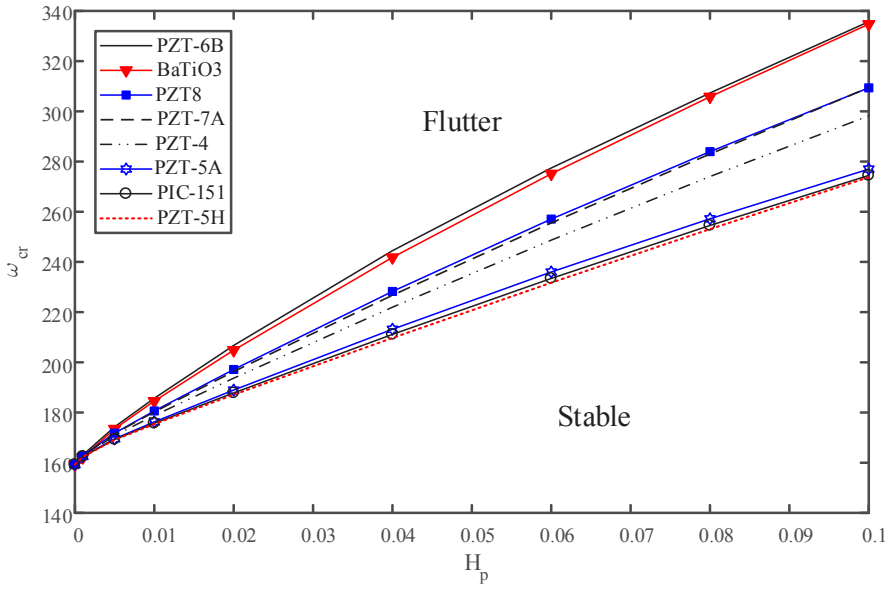

b)

Fig. 6. Influence of various piezoelectric materials on the dynamic stability of FG-V plate in closed circuit condition of the piezoelectric layer; (a) Non-dimensional critical aerodynamic pressure and (b) Non-dimensional critical frequency.

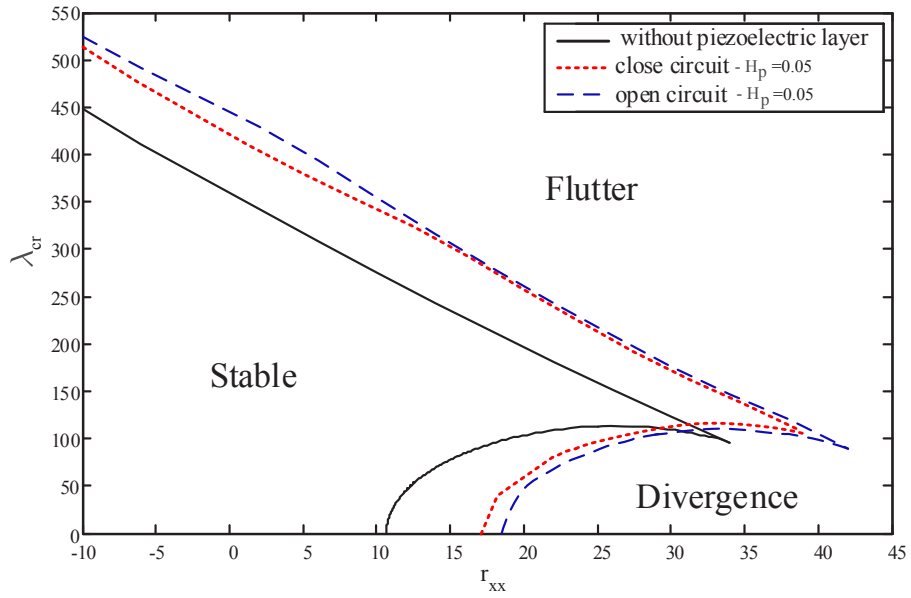

a)

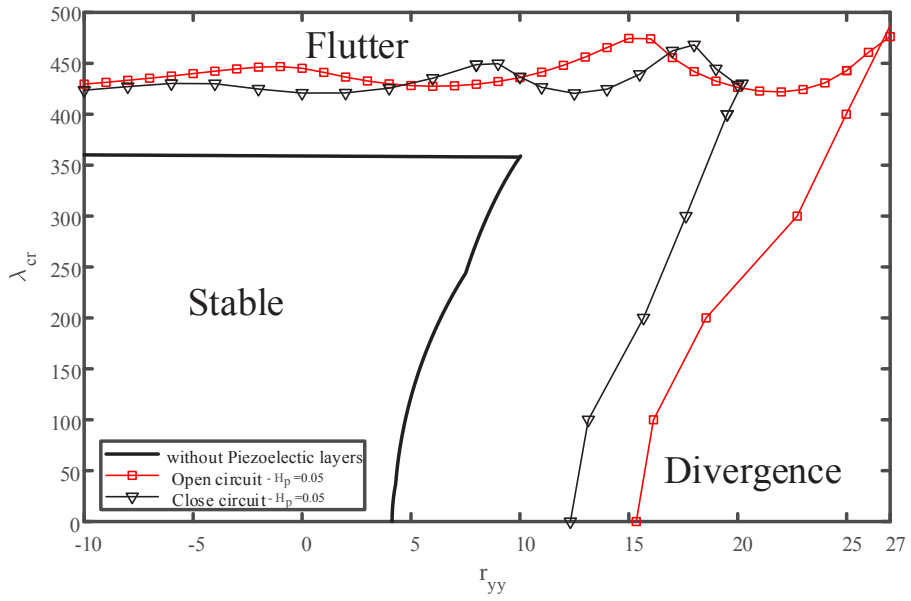

b)

Fig. 7. Effect of non-dimensional in-plane force on the stability boundaries of UD plate enclosed by piezo-electric layers; (a) Non-dimensional in-plane force in x direction and (b) Non-dimensional in-plane force in y direction.

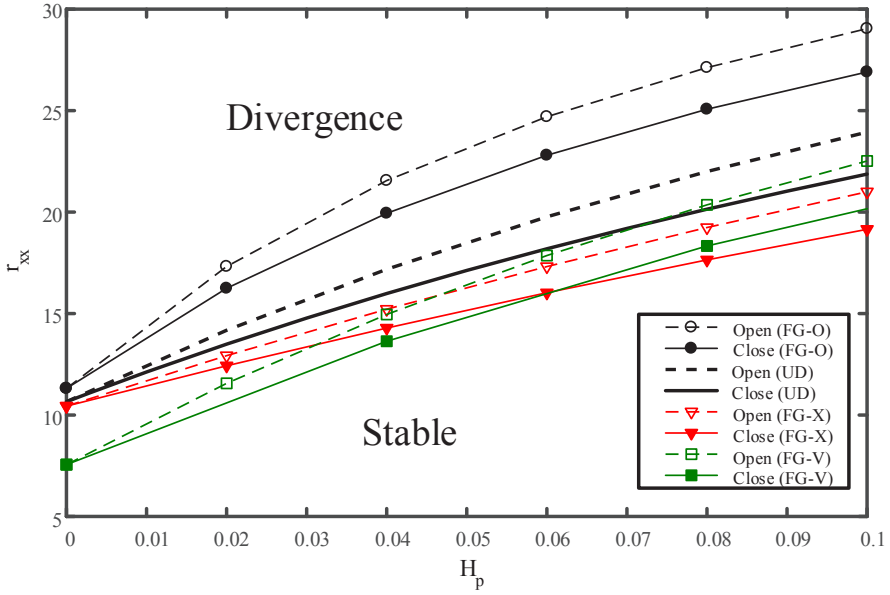

a)

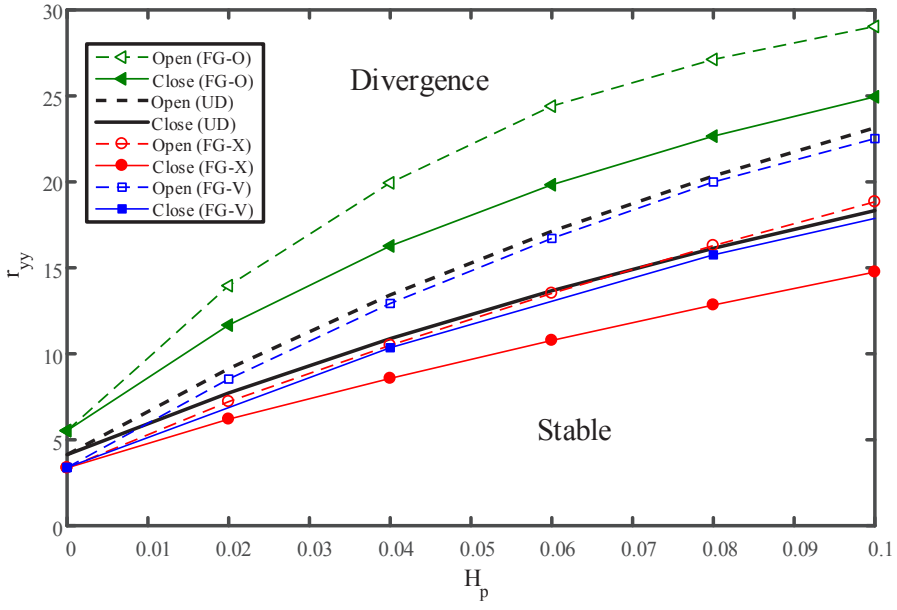

b)

Fig. 8. Effect of non-dimensional piezoelectric thickness on the static stability boundary of FG-CNTRC plate integrated with piezoelectric layers for $\lambda = 0$; (a) Critical non-dimensional in-plane force in x direction and (b) Critical non-dimensional in-plane force in y direction.

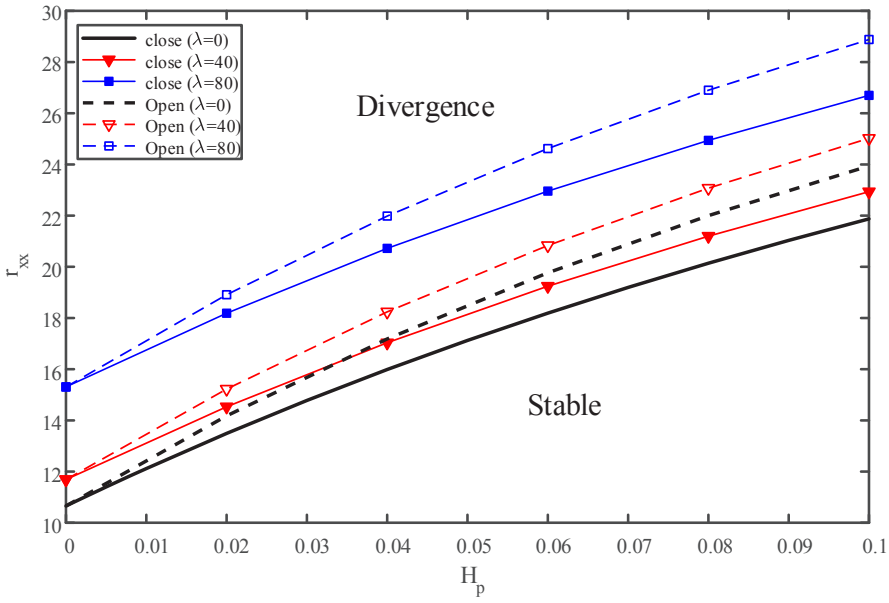

a)

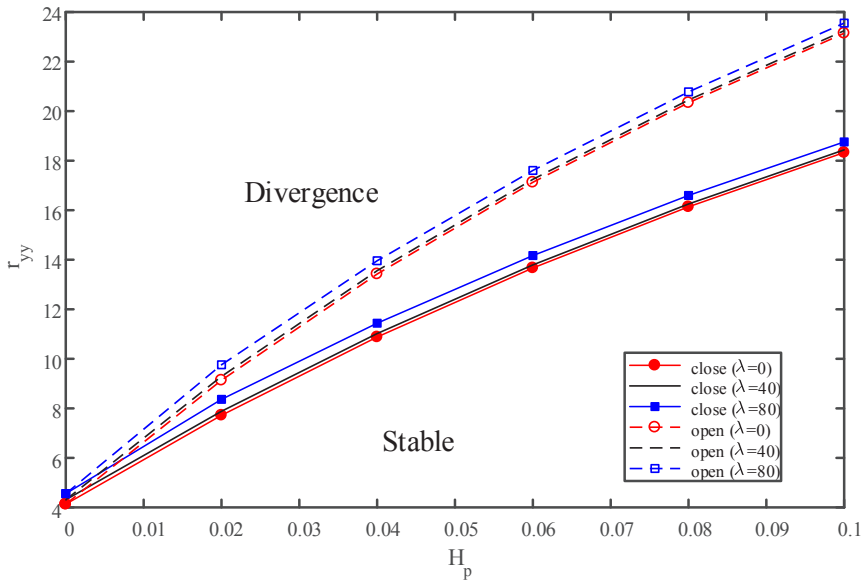

b)

Fig. 9. Variation of critical in-plane force versus the non-dimensional piezoelectric thickness of UD plate enclosed by piezoelectric layers for various aerodynamic pressure; (a) Critical non-dimensional in-plane force in x direction and (b) Critical non-dimensional in-plane force in y direction.

FG-X plate and FG-O plate give the largest and smallest critical frequency, respectively. Because the FG-X plate is stiffer than the FG-O plate in flexural vibration mode.

By increasing the CNT volume fraction as long as the non-dimensional piezoelectric thickness is raised, the critical aerodynamic pressure decreases, but the critical frequency is increased.

The open circuit condition of the piezoelectric layer compared to the closed circuit condition gives the largest dynamic and static stability region. Because, an open circuit boundary condition transforms the electric potential during vibration into mechanical energy, while a close circuit discharges electric potential.

With the increase of non-dimensional piezoelectric thickness, critical in-plane force is increased.

Appendix A

$$\begin{aligned}
&\left(A_1,A_2,A_3\right)=\int_{-\frac{h}{2}}^{\frac{h}{2}}\frac{E_{11}}{1-\nu_{12}\nu_{21}}\left(1,z,z^2\right)dz,\quad \left(B_1,B_2,B_3\right)=\int_{-\frac{h}{2}}^{\frac{h}{2}}\frac{E_{22}}{1-\nu_{12}\nu_{21}}\left(1,z,z^2\right)dz\\
&\left(C_1,C_2,C_3\right)=\int_{-\frac{h}{2}}^{\frac{h}{2}}G_{12}\left(1,z,z^2\right)dz,\quad \left(A_{11}^{'},A_{12}^{'}\right)=2\int_{\frac{h}{2}}^{\frac{h}{2}+h_p}\left(\bar{C}_{11}^{'},\bar{C}_{12}^{'}\right)dz+\Gamma_1\\
&\left(D_{11}^{'},D_{12}^{'}\right)=2\int_{\frac{h}{2}}^{\frac{h}{2}+h_p}\left(\bar{C}_{11}^{'},\bar{C}_{12}^{'}\right)z^2dz+\Gamma_2,\quad \left(A_{66}^{'},D_{66}^{'}\right)=\int_{\frac{h}{2}}^{\frac{h}{2}+h_p}\left(\bar{C}_{11}^{'}-\bar{C}_{12}^{'}\right)\left(1,z^2\right)dz
\end{aligned}\tag{A.1}$$

Also for close-circuit

$$\zeta_1=\frac{4\bar{e}_{13}h_p}{3},\quad \Gamma_1=\Gamma_2=0 \tag{A.2}$$

$$\mu_1=\frac{4}{3}h_p\Xi_{11},\quad \mu_2=0,\quad \mu_3=2\bar{e}_{31}h_p,\quad \mu_4=\frac{16}{h_p}\bar{\Xi}_{33} \tag{A.3}$$

And for open-circuit we have

$$\zeta_1=\frac{8\bar{e}_{13}\left(3h+h_p\right)}{3},\quad \Gamma_1=2\bar{e}_{13}\frac{h_p}{\bar{\Xi}_{33}},\quad \Gamma_2=\frac{\bar{e}_{13}^2h_p\left(h+h_p\right)\left(2h+h_p\right)}{\bar{\Xi}_{33}} \tag{A.4}$$

$$\mu_1=\frac{16}{3}h_p\Xi_{11},\quad \mu_2=\frac{\bar{e}_{31}\Xi_{11}}{\bar{\Xi}_{33}}\left(\frac{1}{2}hh_p^2+h_p^3\right),\quad \mu_3=2\bar{e}_{31}h_p,\quad \mu_4=\frac{16}{h_p}\bar{\Xi}_{33} \tag{A.5}$$

References

[1] M. Cadek, J. Coleman, V. Barron, K. Hedicke, W. Blau, Morphological and mechanical properties of carbon-nanotube-reinforced semicrystalline and amorphous polymer composites, Applied physics letters, 81(27) (2002) 5123-5125.

[2] E.T. Thostenson, T.-W. Chou, On the elastic properties of carbon nanotube-based composites: modelling and characterization, Journal of Physics D: Applied Physics, 36(5) (2003) 573.

[3] N. Hu, H. Fukunaga, C. Lu, M. Kameyama, B. Yan, Prediction of elastic properties of carbon nanotube reinforced composites, Proceedings of the Royal Society A: Mathematical, Physical and Engineering Sciences, 461(2058) (2005) 1685-1710.

[4] H.-S. Shen, Nonlinear bending of functionally graded carbon nanotube-reinforced composite plates in thermal environments, Composite Structures, 91(1) (2009) 9-19.

[5] P. Zhu, Z. Lei, K.M. Liew, Static and free vibration analyses of carbon nanotube-reinforced composite plates using finite element method with first order shear deformation plate theory, Composite Structures, 94(4) (2012) 1450-1460.

[6] Z. Lei, K. Liew, J. Yu, Buckling analysis of functionally graded carbon nanotube-reinforced composite plates using the element-free kp-Ritz method, Composite Structures, 98 (2013) 160-168.

[7] Z. Lei, K. Liew, J. Yu, Free vibration analysis of functionally graded carbon nanotube-reinforced composite plates using the element-free kp-Ritz method in thermal environment, Composite Structures, 106 (2013) 128-138.

[8] M. Wang, Z.-M. Li, P. Qiao, Semi-analytical solutions to buckling and free vibration analysis of carbon nanotube-reinforced composite thin plates, Composite Structures, 144 (2016) 33-43.

[9] N. Wu, Q. Wang, S. Quek, Free vibration analysis of piezoelectric coupled circular plate with open circuit, Journal of Sound and Vibration, 329(8) (2010) 1126-1136.

[10] M.A. Farsangi, A. Saidi, R. Batra, Analytical solution for free vibrations of moderately thick hybrid piezoelectric laminated plates, Journal of Sound and Vibration, 332(22) (2013) 5981-5998.

[11] Y. Kiani, Free vibration of functionally graded carbon nanotube reinforced composite plates integrated with piezoelectric layers, Computers & Mathematics with Applications, 72(9) (2016) 2433-2449.

[12] L. Zhang, Z. Song, K. Liew, Computation of aerothermoelastic properties and active flutter control of CNT reinforced functionally graded composite panels in supersonic airflow, Computer Methods in Applied Mechanics and Engineering, 300 (2016) 427-441.

[13] B. Selim, L. Zhang, K. Liew, Active vibration control of CNT-reinforced composite plates with piezoelectric layers based on Reddy's higher-order shear deformation theory, Composite Structures, 163 (2017) 350-364.

[14] G. Cheng, Y. Lee, C. Mei, Flow angle, temperature, and aerodynamic damping on supersonic panel flutter stability boundary, Journal of aircraft, 40(2) (2003) 248-255.

[15] H. Navazi, H. Haddadpour, Aero-thermoelastic stability of functionally graded plates, Composite Structures, 80(4) (2007) 580-587.

[16] K.-J. Sohn, J.-H. Kim, Structural stability of functionally graded panels subjected to aero-thermal loads, Composite Structures, 82(3) (2008) 317-325.

[17] M. Hosseini, S. Fazelzadeh, Aerothermoelastic post-critical and vibration analysis of temperature-dependent functionally graded panels, Journal of Thermal Stresses, 33(12) (2010) 1188-1212.

[18] P. Marzocca, S. Fazelzadeh, M. Hosseini, A review of nonlinear aero-thermo-elasticity of functionally graded panels, Journal of Thermal Stresses, 34(5-6) (2011) 536-568.

[19] Z.-G. Song, F.-M. Li, Investigations on the flutter properties of supersonic panels with different boundary conditions, International Journal of Dynamics and Control, 2(3) (2014) 346-353.

[20] S. Fazelzadeh, S. Pouresmaeeli, E. Ghavanloo, Aeroelastic characteristics of functionally graded carbon nanotube-reinforced composite plates under a supersonic flow, Computer Methods in Applied Mechanics and Engineering, 285 (2015) 714-729.

[21] Z. Song, L. Zhang, K. Liew, Aeroelastic analysis of CNT reinforced functionally graded composite panels in supersonic airflow using a higher-order shear deformation theory, Composite Structures, 141 (2016) 79-90.

[22] J. Fidelus, E. Wiesel, F. Gojny, K. Schulte, H. Wagner, Thermo-mechanical properties of randomly oriented carbon/epoxy nanocomposites, Composites Part A: Applied Science and Manufacturing, 36(11) (2005) 1555-1561.

[23] M. Nie, D.M. Kalyon, F.T. Fisher, Interfacial load transfer in polymer/carbon nanotube nanocomposites with a nanohybrid shish kebab modification, ACS applied materials & interfaces, 6(17) (2014) 14886-14893.

[24] K. Liew, Z. Lei, J. Yu, L. Zhang, Postbuckling of carbon nanotube-reinforced functionally graded cylindrical panels under axial compression using a meshless approach, Computer Methods in Applied Mechanics and Engineering, 268 (2014) 1-17.

[25] A. Preumont, Piezoelectric systems, Mechatronics: Dynamics of Electromechanical and Piezoelectric Systems, (2006) 95-130.

[26] P. Lee, W. Lin, Piezoelectrically forced vibrations of rectangular SC-cut quartz plates, Journal of applied physics, 83(12) (1998) 7822-7833.

[27] Q. Wang, S. Quek, C. Sun, X. Liu, Analysis of piezoelectric coupled circular plate, Smart Materials and Structures, 10(2) (2001) 229.

[28] E.H. Dowell, Aeroelasticity of plates and shells, Noordhoff International Publishing, Leyden, 1975.

[29] E.H. Dowell, Nonlinear oscillations of a fluttering plate, AIAA journal, 4(7) (1966).

[30] M. Hosseini, R. Bahaadini, Size dependent stability analysis of cantilever micro-pipes conveying fluid based on modified strain gradient theory, International Journal of Engineering Science, 101 (2016) 1-13.

[31] R. Bahaadini, M. Hosseini, Effects of nonlocal elasticity and slip condition on vibration and stability analysis of viscoelastic cantilever carbon nanotubes conveying fluid, Computational Materials Science, 114 (2016) 151-159.

[32] R. Bahaadini, A.R. Saidi, M. Hosseini, On dynamics of nanotubes conveying nanoflow, International Journal of Engineering Science, 123 (2018) 181-196.

[33] Z.-X. Wang, H.-S. Shen, Nonlinear vibration of nanotube-reinforced composite plates in thermal environments, Computational Materials Science, 50(8) (2011) 2319-2330.

[34] Y. Han, J. Elliott, Molecular dynamics simulations of the elastic properties of polymer/carbon nanotube composites, Computational Materials Science, 39(2) (2007) 315-323.

[35] M. Mohammadzadeh-Keleshteri, H. Asadi, M. Aghdam, Geometrical nonlinear free vibration responses of FG-CNT reinforced composite annular sector plates integrated with piezoelectric layers, Composite Structures, 171 (2017) 100-112.

[36] J. Dugundji, Theoretical considerations of panel flutter at high supersonic Mach numbers, AIAA Journal, 4(7) (1966) 1257-1266.

[37] A.H. Baferani, A. Saidi, E. Jomehzadeh, An exact solution for free vibration of thin functionally graded rectangular plates, Proceedings of the Institution of Mechanical Engineers, Part C: Journal of Mechanical Engineering Science, 225(3) (2011) 526-536.

[38] A.R. Saidi, R. Bahaadini, K. Majidi-Mozafari, On vibration and stability analysis of porous plates reinforced by graphene platelets under aerodynamical loading, Composites Part B: Engineering, 164 (2019) 778-799.

[39] G. Chevallier, S. Ghorbel, A. Benjeddou, A benchmark for free vibration and effective coupling of thick piezoelectric smart structures, Smart Materials and Structures, 17(6) (2008) 065007.

HOW TO CITE THIS ARTICLE

M. Hosseini, K. Majidi Mozafari, Stability Analysis of a Functionally Graded Carbon Nanotube Reinforced Composite Plate Integrated with Piezoelectric Layers under Supersonic Airflow, AUT J. Mech Eng., 6(4) (2022) 525-544.

DOI: 10.22060/ajme.2019.16343.5815